

Laser intracavity absorption magnetometry for optical quantum sensing

J. M. Wollenberg,¹ F. Perona,² A. Palaci,¹ H. Wenzel,² H. Christopher,²
A. Knigge,² W. Knolle,³ J. M. Bopp,^{1,2} and T. Schröder^{1,2,*}

¹*Department of Physics, Humboldt-Universität zu Berlin, Newtonstr. 15, 12489 Berlin, Germany*

²*Ferdinand-Braun-Institut (FBH), Gustav-Kirchhoff-Str. 4, 12489 Berlin, Germany*

³*Leibniz-Institut für Oberflächenmodifizierung e.V., 04318 Leipzig, Germany*

(Dated: January 1, 2026)

Intracavity absorption spectroscopy (ICAS) is a well-established technique for detecting weak absorption signals with ultrahigh sensitivity. Here, we extend this concept to magnetometry using nitrogen-vacancy (NV) centers in diamond. We introduce laser intracavity absorption magnetometry (LICAM), a concept that is in principle applicable to a broader class of optical quantum sensors, including optically pumped magnetometers. Using an electrically driven, edge-emitting diode laser that operates self-sustainably, we show that LICAM enables highly sensitive magnetometers operating under ambient conditions. Near the lasing threshold, we achieve a 475-fold enhancement in optical contrast and a 180-fold improvement in magnetic sensitivity compared with a conventional single-pass geometry. The experimental results are accurately described by a rate-equation model for single-mode diode lasers. From our measurements, we determine a projected shot-noise-limited sensitivity in the $\text{pT}\text{Hz}^{-1/2}$ range and show that, with realistic device improvements, sensitivities down to the $\text{fT}\text{Hz}^{-1/2}$ scale are attainable.

INTRODUCTION

Optical quantum sensors, including optically pumped magnetometers (OPMs) and nitrogen-vacancy (NV^-) centers in diamond, represent a promising platform for biomedical sensing applications, due to their ability to detect magnetic fields under ambient conditions [1, 2]. OPMs rely on atomic vapors and achieve ultrahigh magnetic sensitivities at the attotesla level [1, 3] approaching those of superconducting quantum interference devices [4] and enabling wearable, yet bulky, and mobile platforms for magnetoencephalography [5], magnetocardiography [6] and magnetomyography [7]. Further reduction of sensor footprints leads to reduced sensitivities as a result of unavoidable lower active sensing volumes and therefore requires compensation schemes to maintain high sensitivities [8]. A promising approach to overcome this limitation is the use of optical cavities to enhance light-matter interaction, which has been demonstrated, yet with insufficient sensitivity enhancements [9].

An alternative sensing platform are NV^- -based sensors, for which photonic integration is more advanced and which offer high sensitivity to magnetic, electric fields, and to temperature over a broad frequency range from DC to GHz [10–13]. Diamond as a host material offers exceptional biocompatibility making NV^- sensors highly attractive for diverse research fields and applications in life sciences, material sciences and more [14–16]. NV^- -based quantum sensors have demonstrated key milestones in biomedical sensing, including the detection of a single neuron's action potential [17] and millimeter-scale magnetocardiography [18]. In parallel, major advances have been made toward on-chip integration, fiber packaging, and scalable architectures [19–22].

Despite these achievements, significant sensitivity enhancements are still required to make use of integrated NV^- -sensors for high-demanding biomedical applications such as magnetoencephalography. Similar to OPMs, a viable approach is the use of an optical cavity to enhance sensitivities. Cavity-based implementations have been successfully demonstrated for NV^- ensembles [23, 24]. Nevertheless, these methods have so far not reached fundamental sensitivity limits.

One of the most sensitive spectroscopic techniques for enhancing weak absorption signals is intracavity absorption spectroscopy, in which the spectrum of a laser with a broadband gain profile is highly responsive to frequency-dependent losses in the resonator [25–27]. Sensitivity enhancements up to seven orders of magnitude have been demonstrated [28].

In this work, we combine the principles of intracavity absorption spectroscopy and laser threshold magnetometry [29], demonstrating laser intracavity absorption magnetometry (LICAM) to improve the sensitivity of transmission-based optical quantum sensors using a self-sustained infrared external-cavity diode laser (ECDL). Laser threshold magnetometry was proposed to improve the sensitivity of NV^- -based magnetometers. It exploits a magnetic-field-dependent optical *gain* provided by the NV^- triplet transition inside a laser resonator. When operated close to the lasing threshold, this additional gain can push the laser above threshold, potentially enabling near-unity spin contrast and high magnetic sensitivities [29]. Numerical studies have extended this concept to absorption-based schemes mediated by infrared absorption of the NV^- singlet transition [30], as well as off-resonant pump absorption of the triplet transition [31, 32]. More recently, schemes at the laser threshold have been demonstrated experimentally for both stimulated emission of the visible transition [33, 34] and infrared absorption [35]. These implementations have relied on vertical external-cavity surface-emitting diode lasers, which require optical seeding with high pump powers,

* Corresponding author: tim.schroeder@physik.hu-berlin.de

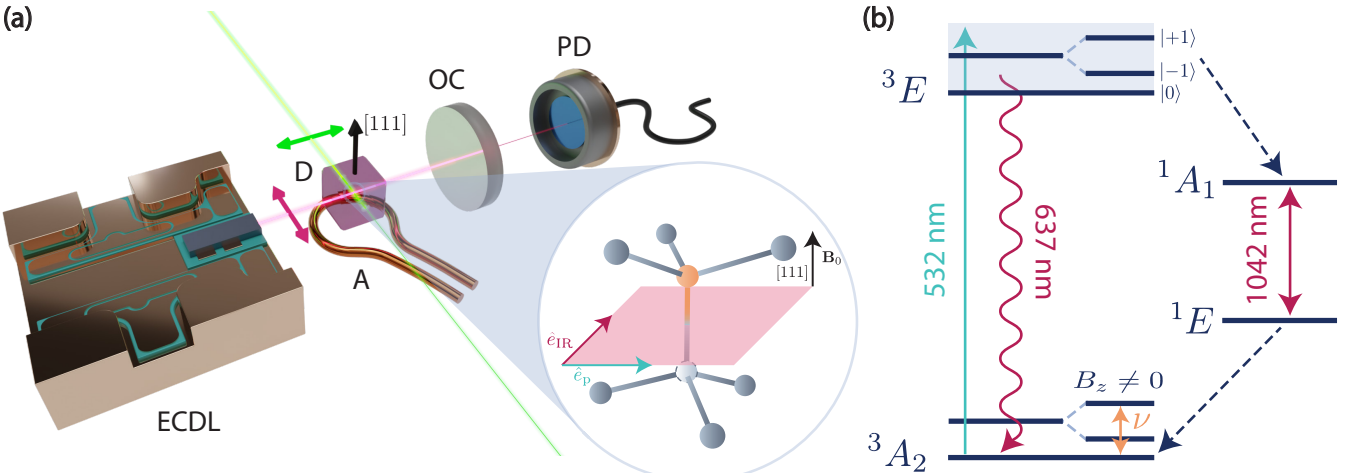


FIG. 1: (a) Schematic of the LICAM setup. An external-cavity diode laser (ECDL) provides optical gain at 1042 nm. A collimating lens (not shown) directs the edge emission through the diamond (D), which is optically pumped at 532 nm. The diamond is cut along the [111] crystal axis (black arrow), which enables perfect cross-sectioning of the linearly polarized pump and probe beams with the [111] NV⁻ resonances. A coupling mirror (OC) closes the cavity, and the optical output power is detected by a photodiode (PD). Magnetic resonances are driven by MW radiation from the antenna (A). (b) Simplified NV⁻ energy level scheme. The ground-state triplet manifold 3A_2 is off-resonantly excited to the excited-state manifold 3E , which fluoresces in red while predominantly preserving the spin state. An external magnetic field lifts the degeneracy of the Zeeman sublevels $|\pm 1\rangle_{ms}$, allowing selective excitation by resonant MW fields of frequency ν . From the excited state, these sublevels preferentially decay via nonradiative intersystem crossing into the singlet state 1A_1 , involving an optical transition at 1042 nm. Probing this transition enables optical detection of the magnetic resonances.

thereby limiting scalability and integration.

In contrast, our LICAM sensor enables a compact, self-contained, and power-efficient magnetometer design with prospects for on-chip integration. We benchmark LICAM against an equivalent single-pass configuration and demonstrate up to a 475-fold enhancement of the optically detected spin contrast and a 180-fold improvement in magnetic sensitivity. Importantly, general enhancements are not only achieved near the lasing threshold but also well above it. We model LICAM using single-mode diode laser rate equations and find excellent agreement with our experimentally determined enhancement factors. Using realistic parameters in our model we determine operational requirements for reaching magnetic sensitivities on the femtotesla level.

RESULTS

The LICAM sensor consists of an electrically driven ECDL incorporating a diamond sample that is part of the optical feedback path in the cavity (see FIG. 1). The laser emission wavelength can be tuned to match the NV⁻ singlet absorption line at 1042 nm, while the diamond is pumped perpendicularly with a 532 nm laser. A microwave (MW) field drives the NV⁻ spin transitions, and sinusoidal frequency modulation of the MW signal enables lock-in detection of optically detected magnetic resonances (ODMRs) through the optical output of the cavity. Varying the ECDL gain current (FIG. 2(a)) allows to study spin contrast and magnetic sensitivity around and above the lasing threshold (for details see **Materials and Methods**).

Enhancement of spin contrast

FIG. 2(b) shows the spin contrast as a function of gain current. The spin contrast sharply increases from about 4×10^{-5} below the lasing threshold to 1.8×10^{-2} at the threshold. Increasing the gain current above the threshold leads to a rapid contrast decrease saturating at about 3×10^{-4} . To benchmark the LICAM performance, we perform conventional single-pass infrared absorption measurements under identical conditions, with the diamond placed outside the cavity. In this configuration, the contrast remains constant at a mean value of 3.8×10^{-5} , independent of the gain current. This behaviour is expected, as the spin contrast does not depend on the probe power [21]. We note that the LICAM contrast below threshold approaches the single-pass contrast, confirming that measurement parameters including the active sensing volume are equivalent in both configurations. Comparing to the single-pass contrast, the LICAM contrast reveals a 475-fold enhancement at the lasing threshold. Moreover, the measured enhancement as a function of gain current agrees excellently with simulations based on single-mode diode-laser rate equations (see section **simulation**). Notably, LICAM yields contrast enhancements not only at the lasing threshold but also well above it, maintaining roughly an order-of-magnitude improvement.

Enhancement of magnetic sensitivity

From fits of the ODMR traces the shot-noise limited sensitivity (SNLS) is calculated using equation (1). FIG. 3(a) shows the result for LICAM and single-pass as a

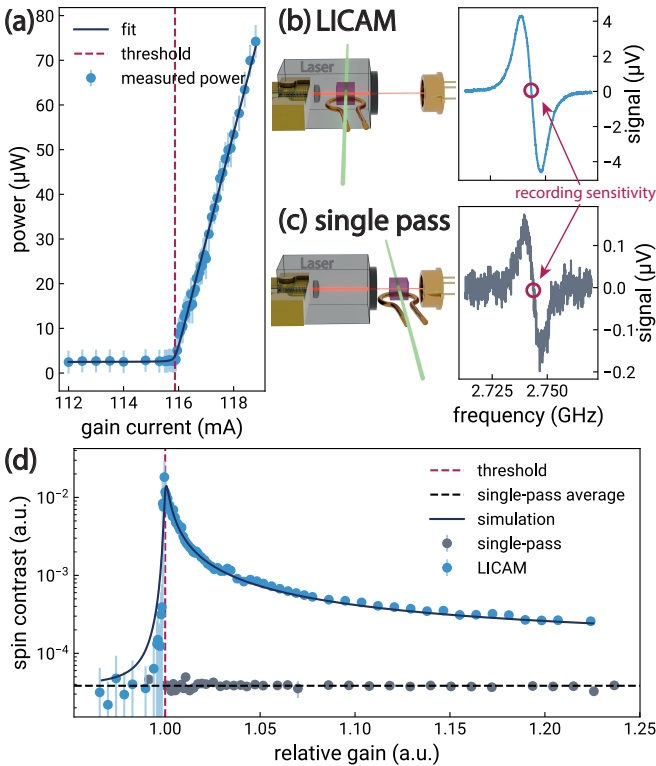


FIG. 2: (a) Characteristic laser output curve of the LICAM sensor, showing a threshold at 116 mA (red dashed line). (b) LICAM configuration and ODMR trace. (c) Single-pass configuration and ODMR trace. ODMR trace in (b) and (c) of the $[111], -1_{\text{ms}}$ -resonance recorded at a relative gain current of 1.03. (d) ODMR contrast as a function of normalized gain current. The gain is normalized to the respective lasing threshold. The solid dark-blue line in (a) represents a fit and in (d) represents a simulation based on a rate equation model for single-mode diode lasers. The dashed black line in (d) indicates the mean contrast value for the single-pass configuration.

function of output power. Approaching the lasing threshold, the SNLS improves rapidly from several hundred $\text{nT Hz}^{-1/2}$ to $1 \text{nT Hz}^{-1/2}$. The optimum value of $500(200) \text{ pT Hz}^{-1/2}$ occurs slightly above the threshold at $P_{\text{IR}} = 5 \mu\text{W}$. Increasing the gain further reduces the shot-noise level due to higher output power, but this improvement is offset by the simultaneous drop in spin contrast, resulting in a net increase in the SNLS. Compared with the single-pass configuration, which follows the expected $1/\sqrt{P_{\text{IR}}}$ dependence, LICAM achieves up to a 400-fold SNLS enhancement. We emphasize that this performance is realized at a low output power of only $5 \mu\text{W}$, whereas conventional optical absorption magnetometers typically operate at power levels of several milliwatts [36]. We measure the magnetic sensitivity of the sensor in the zero-crossing points of the ODMR traces (as shown in FIG. 2(b) and (c)) by recording noise floors. FIG. 3(c) shows the measured sensitivities as a function of gain current. In the single-pass configuration, the sensitivity reaches approximately $1 \mu\text{T Hz}^{-1/2}$ above threshold — about one order of magnitude above the shot-noise limit — and degrades to $\sim 20 \mu\text{T Hz}^{-1/2}$

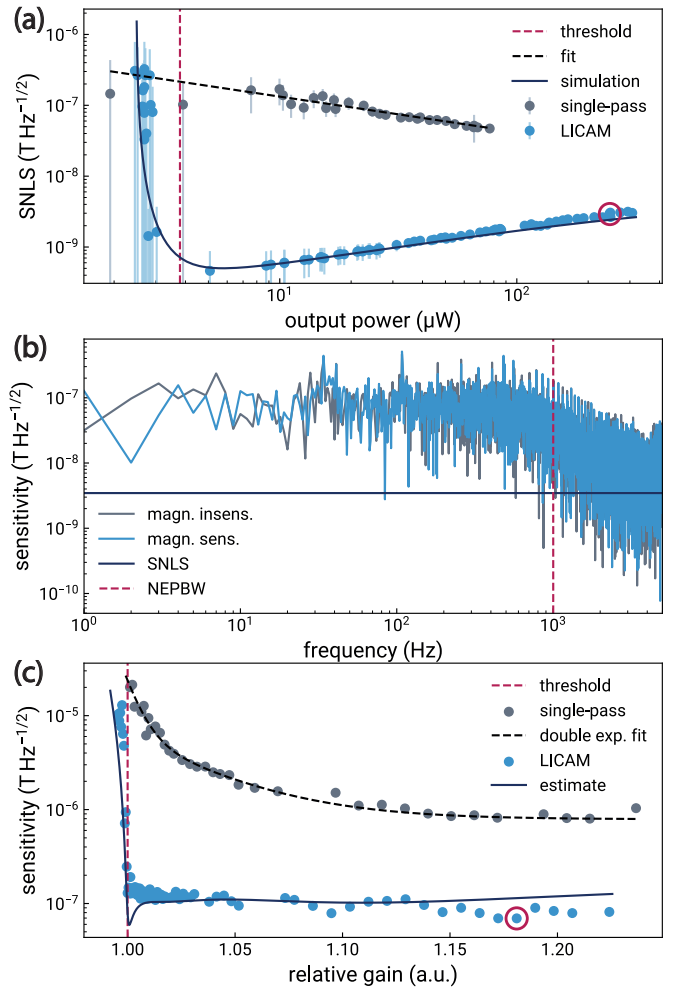


FIG. 3: (a) Shot-noise-limited sensitivity of the single-pass (grey) and LICAM (blue) configurations. The black dashed line represents a fit according to equation (1). The solid blue line shows the result of a simulation (see sec. [simulation](#)), and the red dashed line marks the optical power at the lasing threshold. (b) Sensitivity measurement procedure: A 1 s long time series is recorded and Fourier transformed to obtain the noise floor for the on-resonant (blue) and off-resonant (grey) case. The noise-equivalent power bandwidth is indicated by a red dashed line, and the vertical line marks the shot-noise limit. This measurement corresponds to the circled datapoint in (a) and (c) for a relative gain of 1.18. (c) Measured sensitivity versus gain current for the single-pass (grey) and LICAM (blue) configuration. Single-pass sensitivities were interpolated using a double-exponential decay (black dashed line) and multiplied by the simulated enhancement factor to obtain an estimate for the LICAM sensitivities (dark blue line).

near threshold, suggesting instability caused by increased relative power fluctuations. In contrast, the LICAM sensitivity improves sharply from $\sim 10 \mu\text{T Hz}^{-1/2}$ below threshold to $< 100 \text{nT Hz}^{-1/2}$ above threshold, indicating that the increased power fluctuations are compensated by the contrast enhancement. The optimum sensitivity of $70(2) \text{ nT Hz}^{-1/2}$ is measured at a relative threshold gain of 1.18. To investigate the contribution of magnetic and non-magnetic noise we record an off-resonant noise-floor at this point. FIG. 2(b)

shows the on- and off-resonant noise floor. No significant difference is observed, which indicates that non-magnetic noise dominates the system. Comparing the measured sensitivities with the simulation, we find good agreement above threshold. However near threshold, the measured values exceed predictions by a factor of 2.5 and lack the pronounced drop seen in the simulation (FIG. 3(c)). This discrepancy could arise from thermal fluctuations in the diamond induced by the pump laser, or from mechanical vibrations of the diamond mount. When the diamond is inside the cavity, such fluctuations can increase the phase and amplitude noise of the cavity mode, potentially playing a more significant role near threshold. Nevertheless, an optimal sensitivity enhancement of 180 is achieved at threshold.

Towards femtotesla sensitivities with low power requirements

Having established a validated model that reproduces the experimental results, we now explore the sensitivities achievable assuming realistic parameters reported in the literature. In addition, we assess these sensitivities within practical power constraints. To quantify this, we vary a set of parameters, which we classify into primary parameters - those that directly improve the enhancement - and secondary parameters, which must be optimized for best performance (see supplementary for details).

Our figures of merit are the shot-noise-limited sensitivity η_{SNLS} and the enhancement factor ξ . For a given set of parameters, we compute these quantities from equation (4) as functions of gain current and identify their respective optima (Supplementary FIG. S5). The enhancement factor is always maximized at the lasing threshold and approaches a constant value for higher gain currents, as the gain saturates. The SNLS exhibits a local minimum at the threshold and approaches a slope proportional to $1/\sqrt{P_{\text{IR}}}$ above it. We find that the local SNLS minimum at threshold improves with higher absorption constants $\Delta\alpha$ and lower differential gain g , albeit at the cost of higher drive currents (Supplementary FIG. S6). However, in realistic environments — particularly for fiber-packaged, scaled-up or miniaturized devices — power limits must be observed. This particularly hinders VECSEL-based gain chips, which require pump lasers with power levels on the order of several watts [30, 35]. In contrast, our ECDL-chip is electrically driven with a gain power consumption of 174 mW operated at the lasing threshold. In the following simulations, we therefore impose a gain current limit of 200 mA, corresponding to the maximum operating current of the ECDL chip. FIG. 4 presents simulations for $\eta_{\text{SNLS}}(I)$ and $\xi(I)$ for different differential gain values with improved parameters. Both the enhancement factor and the SNLS improve as the gain decreases and the threshold current approaches the current limit. For larger g values, where the threshold is reached at much smaller currents, the SNLS at the current limit exceeds the threshold. We systematically investigate this behavior by calculating $\eta_{\text{SNLS}}(I)$ and $\xi(I)$ for varying g and front facet reflectivity R , identifying the optimum operating point within the current limit of $I_c =$

200 mA. Each point is classified according to whether the threshold is not reached, the optimum occurs at the lasing threshold, or the optimum occurs at the current limit. The results of this simulation are shown in FIG. 5.

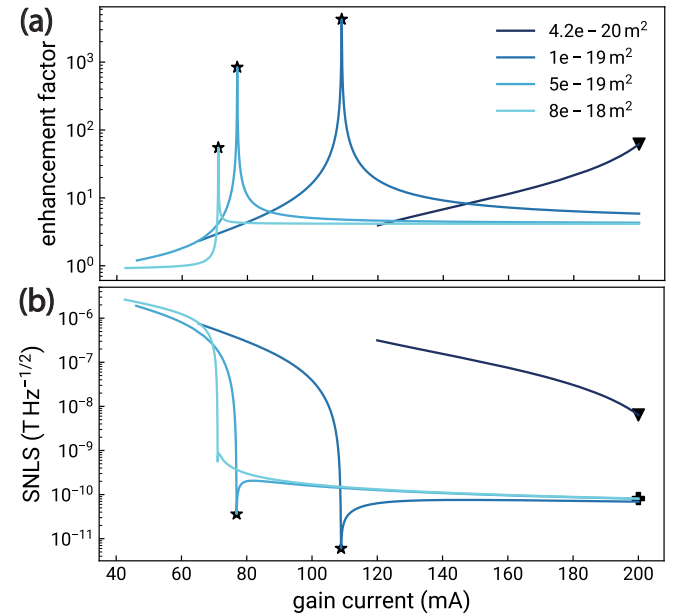


FIG. 4: (a) Simulation of the LICAM enhancement factor $\xi(I)$ with respect to the gain current I for varying differential gain g . (b) Simulation of the shot-noise limited sensitivity η . The black markers highlight if the optimum values were achieved at the lasing threshold (star), above the threshold at the current limit of $I_c = 200$ mA (plus) or if the threshold was not reached (triangle). $R_f = 0.8$, $a = 20 \text{ m}^{-1}$. Other parameters as listed in the supplementary, TAB. I.

We observe a lower limit $g(R)$, below which the system can not reach the lasing threshold. Above this line, threshold operation yields the best performance. Even for small absorption constants of $\Delta\alpha = 0.01 \text{ m}^{-1}$, the simulations predict sensitivities up to $2 \text{ pT Hz}^{-1/2}$ for realistic parameters (Supplementary TAB. I, prosp.). Increasing the absorption to $\Delta\alpha = 20 \text{ m}^{-1}$ improves the SNLS up to $22 \text{ fT Hz}^{-1/2}$. For such high absorption constants, the spin contrast saturates at unity, resulting in moderate enhancement factors $\xi \approx 600$ for $R_f \rightarrow 1$ compared with much larger values ($\xi \approx 2.4 \times 10^4$) obtained for $\Delta\alpha = 0.01 \text{ m}^{-1}$. FIG. 5(e) shows the optimum SNLS as a function of $\Delta\alpha$ for different current limits. In general, higher available current improves the SNLS. We find two scaling regimes: $\eta_{\text{SNLS}} \propto \Delta\alpha^{-1}$ for small absorption constants $\Delta\alpha \lesssim 10^{-2} \text{ m}^{-1}$ and $\eta_{\text{SNLS}} \propto \sqrt{\Delta\alpha}$ for $\Delta\alpha \gtrsim 10^{-1} \text{ m}^{-1}$ where the spin contrast saturates. Overall, our simulations indicate that femtotesla sensitivities are achievable even with the relatively small absorption constant present in this experiment ($\Delta\alpha \approx 3.8 \text{ m}^{-1}$), provided that other key parameters are improved.

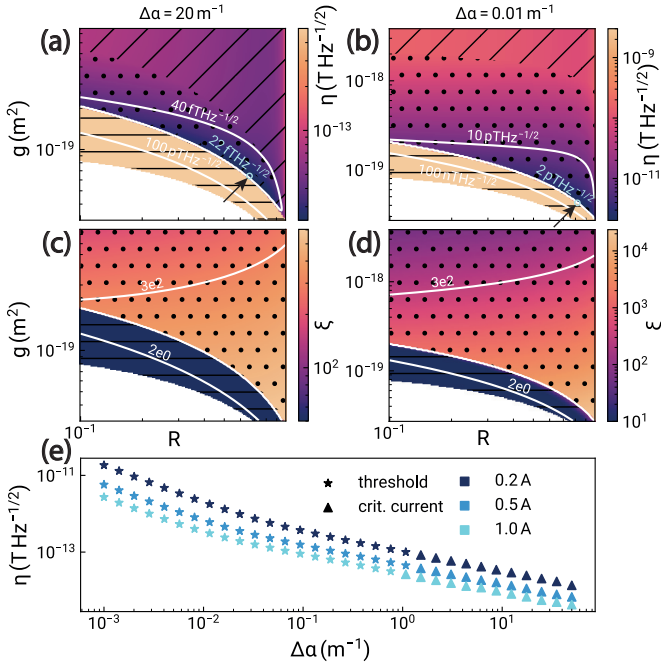


FIG. 5: Simulated optimal values of the enhancement factor $\xi(I)$ and the SNLS $\eta(I)$ with a current limit of $I_c = 200$ mA, with respect to the differential gain g and the front facet reflectivity R_f , using improved parameters (Supplementary TAB. I). (a), (b): Shot-noise limited sensitivity and (c), (d): Enhancement factor for $\Delta\alpha = 20$ m $^{-1}$ and $\Delta\alpha = 0.01$ m $^{-1}$, respectively. White contour lines indicate iso-levels, and the pale blue circles in (a) and (b) the optimum value. Hatchings indicate in which operating regime the optimum occurs: below the lasing threshold (horizontal lines), at the lasing threshold (dots), or at the current limit (diagonal lines). (e) Optimum SNLS as a function of the absorption constant $\Delta\alpha$ for different current limits. The marker shape indicates threshold operation (stars) or operation at the current limit (triangles).

DISCUSSION

We have demonstrated laser intracavity absorption magnetometry (LICAM) for the first time using a self-sustained infrared laser diode system. By comparing the measurements with an equivalent single-pass configuration, we observe a 475-fold enhancement in ODMR contrast and a 180-fold improvement in magnetic sensitivity at the lasing threshold. Unlike in laser threshold magnetometry, we do not observe a shift of the threshold current. Instead, our results are well described as intracavity absorption effects within a laser diode rate-equation model, which fits the experimental data with excellent agreement. Moreover, we show that sensitivity enhancements occur not only at the lasing threshold but also well above it. In this regime, contrast enhancement decreases by approximately an order of magnitude due to gain saturation. However, the increased laser stability well above threshold improves the overall sensitivity obtained from noise-floor measurements on resonance. Our sensor is partially integrated, current driven, and has an active region of about $(300\mu\text{m})^3$. With a total system footprint already below $3 \times 2 \times 2$ cm 3 , it can be further integrated into a compact,

portable device.

Comparing our experimental parameters with those reported in the literature reveals substantial opportunities for optimization. Replacing the current cross-configuration of the infrared and green pump beams with a collinear geometry [36] would significantly increase the absorption constant. Driving the hyperfine transitions could further steepen the ODMR slope. Using an impedance-matched antenna [37] and a doubly resonant cavity design [38] for the green pump light could significantly reduce the power requirements, which are much larger than the electrical gain power of 174 mW in the current configuration ($P_{\text{MW}} = 1.6$ W, $P_{\text{pump}} = 1.4$ W). The DBR grating can be designed to match the NV $^-$ singlet resonance, eliminating the need for temperature control. In a next step, the diamond can be integrated directly on-chip together with the output coupler, removing the lens and thereby reducing additional scattering losses in the cavity. This integration would enable a compact, millimeter-scale sensor architecture. Our simulations indicate that, with optimized yet realistic control and chip parameters, femtotesla shot-noise-limited sensitivities are achievable for moderate absorption constants above 10^{-1} m $^{-1}$.

Experimentally, our measured sensitivity is not limited by magnetic noise but rather by system noise, most likely dominated by power fluctuations and mechanical vibrations of the external cavity. Additional stabilization schemes or the above discussed chip-integration could mitigate these effects. We also emphasize that LICAM can be operated with pulse sequences, enabling quantum sensing protocols that can further boost sensitivity. Finally, LICAM is not restricted to NV $^-$ -based sensors but can be extended to a broad class of optically interactive quantum sensors, including OPMs that rely on absorption or polarization rotation.

A key challenge that remains is increased relative power fluctuations near the lasing threshold. To address this limitation, we propose multi-mode LICAM, which — analogous to multi-mode intracavity absorption spectroscopy [27, 28] — can operate stably far above the lasing threshold. In contrast to single-mode operation, multi-mode LICAM would be inherently robust against broadband cavity losses and fluctuations.

Realizing these improvements would enable magnetometry performance approaching the shot-noise limit, opening novel opportunities for applications in biomedical sensing, material sciences and beyond.

METHODS

Experiment

We use a high pressure high temperature (HPHT) diamond with an NV $^-$ density of approximately 7 ppm. Both ECDL edge facet and diamond facets are antireflection-coated for the target wavelength of 1042 nm. A tunable distributed Bragg reflector (DBR) selects the 1042 nm infrared resonance from the broad emission spectrum of the current-driven InGaAs

gain medium. A lens collimates the edge emission from the gain chip, which then passes through the diamond, behind which a coupling mirror ($R = 0.9$) closes the external cavity. By tuning the gain current and measuring the optical output power of the cavity we obtain the characteristic power-current curve of a single-mode diode laser (see FIG. 2 (a)), with a lasing threshold of $I_{\text{th}} = 116$ mA. The diamond is pumped perpendicularly by a 532 nm green laser, defining an overlap region with the infrared beam that constitutes the active sensing volume. The diamond is cut along the [111]-direction and oriented such that both the infrared and the green laser are linearly polarized in the [111]-plane, maximizing the optical absorption cross-sections. A copper antenna delivers a microwave (MW) signal driving the NV⁻ spin transitions. We apply sinusoidal frequency modulation at 8 kHz with a modulation depth of 4.5 MHz to enable lock-in detection and optimize for the pump and MW powers. Sweeping the carrier frequency at a fixed gain current yields ODMR spectra (Supplementary FIG. S2(a)). A ring magnet is used to split the spin resonances and isolate the ([111], -1_{ms})-resonance which is used for all measurements. We vary the gain current along the characteristic laser curve and monitor the optical output power while simultaneously recording ODMR spectra, from which the spin contrast is extracted by fitting the derivative of a gaussian resonance profile. Further details can be found in the supplementary. From the fits, we extract the ODMR linewidth which, together with the spin contrast and the optical output power P_{IR} , allows to calculate the SNLS of the LICAM-sensor using the standard expression [39, 40]:

$$\eta_{\text{SNLS}} = \sqrt{\frac{e}{8 \ln 2} \frac{1}{\gamma} \frac{\Delta\nu}{C} \sqrt{\frac{E_{\text{IR}}}{P_{\text{IR}}}}}, \quad (1)$$

where γ is the electron gyromagnetic ratio, C the spin contrast, $\Delta\nu$ the ODMR linewidth, and E_{IR} the infrared photon energy. To determine experimental enhancement factors we repeat the measurements in a single-pass configuration, where the diamond is placed outside the cavity and thus, does not contribute optical feedback. To measure the magnetic sensitivity, the carrier frequency is tuned to the ODMR zero-crossing point $\nu_0 = 2.7435$ GHz for each gain current (see FIG. 2(b) and (c)). A 1 s time trace is recorded at a 10 kHz sampling rate and Fourier transformed to obtain the amplitude spectral density (ASD), as shown in FIG. 3.(b). The AC magnetic sensitivity is calculated as the average noise floor in the 1 Hz to 1 kHz bandwidth. To distinguish magnetic from non-magnetic noise sources, the measurement is repeated with an off-resonant carrier frequency $\nu_{\text{off}} = 2.65$ GHz. We interpolate the single-pass sensitivity using a double-exponential decay and scale it by the simulated LICAM enhancement factor to estimate the LICAM sensitivity.

Simulation

To validate our experimental observations of intracavity enhancement of contrast and sensitivity near the lasing threshold, we employ the following rate-equation model for

a single-mode diode laser including spontaneous emission for the average optical power in the cavity P and the excess carrier density N [41, 42]:

$$\begin{cases} \frac{1}{v_g} \frac{dP}{dt} = [\Gamma g(N) - \alpha - \Gamma \sigma N] P + \frac{K v_g \hbar \omega \Gamma r_{\text{sp}}(N)}{l} \\ \frac{dN}{dt} = \frac{I}{e d W l} - R(N) - \frac{\Gamma g(N) P}{\eta_i d W \hbar \omega} \end{cases} \quad (2)$$

Here, $v_g = c/n_g$ is the group velocity, Γ the optical confinement factor, α the total cavity loss absorption constant, σ the cross-section for free carrier absorption, I the injection current, $\omega = 2\pi c/\lambda$, ω and λ the angular frequency and wavelength, e the elementary charge, $\hbar\omega$ the photon energy, d the thickness of the active region, W the width of the active region, l the length of the active region, K the Petermann K-factor, and η_i the internal efficiency. By linearizing the gain $g(N)$, the spontaneous emission $r_{\text{sp}}(N)$, and the recombination rate $R(N)$ around the threshold carrier density N_{th} , equation (2) can be solved analytically for $P_{\alpha}(I)$ (Supplementary equation (8)). This linearization substantially reduces computational cost, allowing efficient fitting routines and large-scale parameter sweeps that would otherwise require numerical integration of equation (2). The optical power exciting the cavity through the front facet and detected by the photodiode is given by [41, 43]:

$$P_{\alpha}^{(\text{out})}(I) = P_{\text{sp}} - \frac{P_{\alpha}(I)}{2} \ln(R_r R_f) \left[1 + \frac{1 - R_f}{1 - R_r} \sqrt{\frac{R_f}{R_r}} \right]^{-1}, \quad (3)$$

with R_r and R_f denoting the rear and front reflectivities of the cavity, respectively. We account for background spontaneous emission P_{sp} into non-lasing modes that are still detected by the photodiode and contribute to the single-pass optical depth τ_r . By combining equations (2) and (3), we extract η_i , P_{sp} and N_{th} from a fit to the characteristic curve shown in FIG. 2(a). The on-resonant absorption constant $\Delta\alpha$ is derived from the measured single-pass spin contrast C_{sp} , assuming that the optical depth of the overlap region on resonance is equivalent in the LICAM configuration. This enables calculation of the on-resonant LICAM output power $P_{\alpha+\Delta\alpha}(I)$ (see supplementary). Following [44], the intracavity enhancement can be described in terms of an effective optical path length that increases the optical depth:

$$\tau_{\text{eff}}(I) = \tau_r + \ln \left(\frac{P_{\alpha}(I)}{P_{\alpha+\Delta\alpha}(I)} \right). \quad (4)$$

Using equation (4), we calculate the LICAM contrast $C(I) = 1 - \exp\{-\tau_{\text{eff}}(I)\}$, the enhancement factor $\xi(I) = \tau_{\text{eff}}(I)/\tau_r$, and the LICAM shot-noise-limited sensitivity using $P_{\alpha+\Delta\alpha}(I)$ and $C(I)$ in equation (1). The results of these simulations are shown in FIGs. 2.(d) and 3.(a). We find excellent agreement with the experimental data, confirming that the rate-equation model (equation (2)),

together with the applied linearization, adequately describes the LICAM-enhancement of both ODMR contrast and magnetic sensitivity. All simulation parameters are listed in the supplementary, TAB. I.

ACKNOWLEDGEMENT

The authors acknowledge Viviana Villafane for annealing the samples, Peter Ressel and Uwe Sprengler for AR coating the side facets of the sample, Christof Zink for measuring the emission profile of the ECDL chip, and Tommaso Pernigolato for the tri-acid boiling. We thank Sascha Neinert and Kirti Vardhan for a fruitful discussion related to OPMs.

This project is funded by the German Federal Ministry of Research, Technology and Space (BMFTR) within the

“DiNOQuant” project (No. 13N14921), the European Research Council within the ERC Starting Grant “QUREP” (No. 851810), and the Einstein Research Unit “Perspectives of a quantum digital transformation: Near-term quantum computational devices and quantum processors”.

J.W., F.P. and T.S. developed the concept of the LICAM-sensor. J.W. and F.P. designed the experiment. J.W. and A.P. performed the measurements, J.W. analyzed the data. A.P. performed and analyzed the measurements for the sensitivity optimization and the sensor demonstration. H.W. provided the rate equation model, simulation parameters for the ECDL-chip and supported the simulations done by J.W. H.C. und A.K. provided the ECDL-chip. W.K. carried out the electron irradiation of the diamond sample. J.M.B. developed the software platform for the experiments and provided helpful discussions of the experimental data. J.W., A.P. and T.S. wrote the manuscript. All authors contributed to the writing.

[1] D. Budker and M. Romalis, *Nature Physics* **3**, 227 (2007).

[2] N. Aslam, H. Zhou, E. K. Urbach, M. J. Turner, R. L. Walsworth, M. D. Lukin, and H. Park, *Nature Reviews Physics* **5**, 157 (2023).

[3] H. B. Dang, A. C. Maloof, and M. V. Romalis, *Applied Physics Letters* **97**, 10.1063/1.3491215 (2010).

[4] R. K. Dumas and T. Hogan, in *Magnetic Measurement Techniques for Materials Characterization*, edited by B. Dodrill and V. Franco (Springer, Cham, 2021) pp. 39–62.

[5] E. Boto, N. Holmes, J. Leggett, G. Roberts, V. Shah, S. S. Meyer, L. D. Muñoz, K. J. Mullinger, T. M. Tierney, S. Bestmann, G. R. Barnes, R. Bowtell, and M. J. Brookes, *Nature* **555**, 657 (2018).

[6] D. Escalona-Vargas, A. Ramirez, E. R. Siegel, E. H. Bolin, and H. Eswaran, *Scientific Reports* **15**, 7236 (2025).

[7] S. Nordenström, V. Lebedev, S. Hartwig, M. Kruse, J. Marquetand, P. Broser, and T. Middelmann, *Scientific Reports* **14**, 18960 (2024).

[8] M. W. Mitchell and S. Palacios Alvarez, *Reviews of Modern Physics* **92**, 021001 (2020).

[9] H. Crepaz, L. Y. Ley, and R. Dumke, *Scientific Reports* **5**, 15448 (2015).

[10] J. M. Taylor, P. Cappellaro, L. Childress, L. Jiang, D. Budker, P. R. Hemmer, A. Yacoby, R. Walsworth, and M. D. Lukin, *Nature Physics* **4**, 810 (2008).

[11] F. Dolde, H. Fedder, M. W. Doherty, T. Nöbauer, F. Rempp, G. Balasubramanian, T. Wolf, F. Reinhard, L. C. L. Hollenberg, F. Jelezko, and J. Wrachtrup, *Nature Physics* **7**, 459 (2011).

[12] G. Kucsko, P. C. Maurer, N. Y. Yao, M. Kubo, H. J. Noh, P. K. Lo, H. Park, and M. D. Lukin, *Nature* **500**, 54 (2013).

[13] I. Jakobi, P. Neumann, Y. Wang, D. B. R. Dasari, F. El Hallak, M. A. Bashir, M. Markham, A. Edmonds, D. Twitchen, and J. Wrachtrup, *Nature Nanotechnology* **12**, 67 (2017).

[14] D. R. Glenn, D. B. Bucher, J. Lee, M. D. Lukin, H. Park, and R. L. Walsworth, *Nature* **555**, 351 (2018).

[15] F. Casola, T. van der Sar, and A. Yacoby, *Nature Reviews Materials* **3**, 10.1038/natrevmats.2017.88 (2018).

[16] Z. Qiu, A. Hamo, U. Vool, T. X. Zhou, and A. Yacoby, *npj Quantum Information* **8**, 1 (2022).

[17] J. F. Barry, M. J. Turner, J. M. Schloss, D. R. Glenn, Y. Song, M. D. Lukin, H. Park, and R. L. Walsworth, *Proceedings of the National Academy of Sciences of the United States of America* **113**, 14133 (2016).

[18] K. Arai, A. Kuwahata, D. Nishitani, I. Fujisaki, R. Matsuki, Y. Nishio, Z. Xin, X. Cao, Y. Hatano, S. Onoda, C. Shinei, M. Miyakawa, T. Taniguchi, M. Yamazaki, T. Teraji, T. Ohshima, M. Hatano, M. Sekino, and T. Iwasaki, *Communications Physics* **5**, 200 (2022).

[19] M. I. Ibrahim, C. Foy, D. R. Englund, and R. Han, *IEEE Journal of Solid-State Circuits* **56**, 1001 (2021).

[20] F. M. Stürner, A. Brenneis, T. Buck, J. Kassel, R. Röller, T. Fuchs, A. Savitsky, D. Suter, J. Grimmel, S. Hengesbach, M. Förtzsch, K. Nakamura, H. Sumiya, S. Onoda, J. Isoya, and F. Jelezko, *Advanced Quantum Technologies* **4**, 2000111 (2021).

[21] J. M. Bopp, H. Conradi, F. Perona, A. Palaci, J. Wollenberg, T. Flisgen, A. Liero, H. Christopher, N. Keil, W. Knolle, A. Knigge, W. Heinrich, M. Kleinert, and T. Schröder, *Physical Review Applied* **23**, 034024 (2025).

[22] O. Gazzano and C. Becher, *Physical Review B* **95**, 10.1103/PhysRevB.95.115312 (2017).

[23] K. Jensen, N. Leefer, A. Jarmola, Y. Dumeige, V. M. Acosta, P. Kehayias, B. Patton, and D. Budker, *Physical review letters* **112**, 160802 (2014).

[24] G. Chatzidrosos, A. Wickenbrock, L. Bougas, N. Leefer, T. Wu, K. Jensen, Y. Dumeige, and D. Budker, *Physical Review Applied* **8**, 044019 (2017).

[25] L. A. Pakhomycheva, E. Sviridenkov, A. Suchkov, L. Titova, and S. Churilov, *JETP Lett.* **12**, (1970).

[26] H. Kimble, *IEEE Journal of Quantum Electronics* **16**, 455 (1980).

[27] P. Fjodorow, *Applied Physics B* **130**, 1 (2024).

[28] V. M. Baev, T. Latz, and P. E. Toschek, *Applied Physics B* **69**, 171 (1999).

[29] J. Jeske, J. H. Cole, and A. D. Greentree, *New Journal of Physics* **18**, 013015 (2016).

[30] Y. Dumeige, J.-F. Roch, F. Bretenaker, T. Debuisschert, V. Acosta, C. Becher, G. Chatzidrosos, A. Wickenbrock, L. Bougas, A. Wilzewski, and D. Budker, *Optics express* **27**, 1706 (2019).

- [31] S. Raman Nair, L. J. Rogers, X. Vidal, R. P. Roberts, H. Abe, T. Ohshima, T. Yatsui, A. D. Greentree, J. Jeske, and T. Volz, *Nanophotonics* **9**, 4505 (2020).
- [32] J. L. Webb, A. F. L. Poulsen, R. Staacke, J. Meijer, K. Berg-Sørensen, U. L. Andersen, and A. Huck, *Physical Review A* **103**, 10.1103/PhysRevA.103.062603 (2021).
- [33] F. A. Hahl, L. Lindner, X. Vidal, T. Luo, T. Ohshima, S. Onoda, S. Ishii, A. M. Zaitsev, M. Capelli, B. C. Gibson, A. D. Greentree, and J. Jeske, *Science advances* **8**, eabn7192 (2022).
- [34] L. Lindner, F. A. Hahl, T. Luo, G. N. Antonio, X. Vidal, M. Rattunde, T. Ohshima, J. Sacher, Q. Sun, M. Capelli, B. C. Gibson, A. D. Greentree, R. Quay, and J. Jeske, *Science advances* **10**, eadj3933 (2024).
- [35] N. S. Gottesman, M. A. Slocum, G. A. Severson, M. Wolf, M. L. Lukowski, C. Hessenius, M. Fallahi, and R. G. Bedford, *Applied Physics Letters* **124**, 10.1063/5.0174282 (2024).
- [36] A. Tayefeh Younesi, M. Omar, A. Wickenbrock, D. Budker, and R. Ulbricht, *Physical Review Applied* **23**, 054019 (2025).
- [37] O. R. Opaluch, N. Oshnik, R. Nelz, and E. Neu, *Nanomaterials* (Basel, Switzerland) **11**, 10.3390/nano11082108 (2021).
- [38] Y. Dumeige, M. Chipaux, V. Jacques, F. Treussart, J.-F. Roch, T. Debuisschert, V. M. Acosta, A. Jarmola, K. Jensen, P. Kehayias, and D. Budker, *Physical Review B* **87**, 10.1103/PhysRevB.87.155202 (2013).
- [39] A. Dréau, M. Lesik, L. Rondin, P. Spinicelli, O. Arcizet, J.-F. Roch, and V. Jacques, *Physical Review B* **84**, 10.1103/PhysRevB.84.195204 (2011).
- [40] V. M. Acosta, E. Bauch, A. Jarmola, L. J. Zipp, M. P. Ledbetter, and D. Budker, *Applied Physics Letters* **97**, 174104 (2010).
- [41] M. Kastner, H. Wenzel, J. Schwarz, A. Knigge, and G. Tränkle, *Semiconductor Science and Technology* **34**, 035019 (2019).
- [42] H. Wenzel, M. Kantner, M. Radziunas, and U. Bandelow, *Applied Sciences* **11**, 6004 (2021).
- [43] L. A. Coldren, S. W. Corzine, and M. L. Mašanović, *Diode Lasers and Photonic Integrated Circuits* (Wiley, 2012).
- [44] B. Scherer, W. Salzmann, J. Wöllensteiner, and M. Weidmüller, *Applied Physics B* **96**, 281 (2009).